Modeling the perturbation growth in an acoustically excited plane jet

Péter Tamás Nagy, and György Paál

Modeling the perturbation growth in an acoustically excited plane jet

Péter Tamás Nagy[a) and György Paál[b)
Department of Hydrodynamic Systems, Faculty of Mechanical Engineering, Budapest University of Technology and Economics, Műegyetem rkp. 3, Budapest H-1111, Hungary

Four methods of varying complexity to investigate jet instability were tested on a plane jet and compared with CFD results. A unified treatment that includes the acoustic excitation in an incompressible simulation was developed. It turned out that the more sophisticated methods have no real advantage over the well-established Orr-Sommerfeld and Rayleigh equations. A new mode with extremely high growth rates in the vicinity of the nozzle exit was discovered. *Published by AIP Publishing.*
https://doi.org/10.1063/1.4993558

I. INTRODUCTION

The physical modeling of flue instruments is a challenging task. Although the research began in the late 19th century, many aspects are still unclear. An excellent review of recent lumped models was written by Fabre and Hirschberg.[8] They presented various techniques and attempts to describe the hydrodynamic amplification of vorticity inside the jets, the sound generation process, and the receptivity of the jet. They draw the conclusion that although the lumped models explain some global observations, they do not fully reveal the physical mechanisms. In our paper, an attempt is made to improve these models focusing only on the growth of perturbations in the initial linear domain of the jet.

Rayleigh[21] was the first author to describe the growth of perturbation velocity in jets. He derived the famous Rayleigh equation and solved it for a discontinuous velocity profile that is a crude model of the shear layer. The next essential step in the description of planar jets was the work of Bickley.[4] He derived an analytical formula (Bickley-profile) for the velocity field generated by an infinitely long line momentum source, assuming self-similarity. The validity of the Bickley velocity profile was confirmed by experiments. Later, Savic[23] solved the Rayleigh equation for the Bickley profile neglecting the streamwise variation of the flow field. Curle[6] and Tatsumi and Kakutani[27] solved the Orr-Sommerfeld equation and published the neutral stability curve for the same velocity profile. Sato[22] also solved the Orr-Sommerfeld equation but he used the mean velocity profiles from his measurements instead of the theoretical Bickley-profile. Later, several attempts were made to extend the Orr-Sommerfeld equation. Varapaev *et al.*[30] derived a modified Orr-Sommerfeld equation, which considered the transversal velocity component, using the stream function. A similar concept was followed by Bajaj and Garg,[3] who also took into account the transversal mean velocity. The investigation of an arbitrary flow needs less effort by their method since instead of the stream function they used the mean transversal velocity profile in the

equation, which can be easily exported from numerical simulations. Garg[10] continued the research and developed a weakly nonparallel model that took into consideration the effects of the transversal velocity component and the streamwise variations of the basic flow, the disturbance amplitude, the wave number, and the spatial growth rate. In this model, the growth rate depends not only on the streamwise co-ordinates but also on transversal co-ordinate and the particular flow variable.

Fletcher and Thwaites[9] set up a model in which they defined the critical distance x_c. Before this distance, the growth can be modeled with Rayleigh's method of the discontinuous shear layer and beyond that with the solution of Savic for the Bickley-profile. Actually, both solutions are based on the Rayleigh-equation, which neglects viscosity for the perturbation modes and is valid at high Reynolds-number (for the Bickley-jet $Re > 200$[6]). Motivated by organ pipe jet research, Nolle[19] solved the Rayleigh equation numerically for the Bickley jet and validated it by measurements. He suggested that the growth of disturbances should be modeled spatially instead of temporally. He also proposed an analytical formula to describe jets in the vicinity of the nozzle, whose stability properties were investigated in our previous work.[17] Atassi and Lueptow[2] developed a non-linear "long wave" model. Their model describes the initially exponential and further downstream linear growth of perturbations. The paper deals with asymmetric mean velocity profiles as well, approximated by piecewise linear functions. In the same year, Jo and Kim[14] studied the growth of the perturbation field in the vicinity of the orifice. They introduced a new non-dimensionalization technique. They determined the location from which the Bickley profile describes flows with parabolic and top-hat exit velocity profiles well. They also compared results of local and non-local stability analysis. They found that local techniques provide almost identical results, if the Reynolds-number (defined in the same way as here) is larger than 100. However, the presence of the wall around the jet was neglected in their work. It probably leads to the underestimation of the growth of varicose modes.[17] This can be a problem when modeling an instrument with a short flue channel, where these modes are observable.[24]

a)Electronic mail: pnagy@hds.bme.hu
b)Electronic mail: paal@hds.bme.hu

29, 114102-1

Dequand *et al.*[7] modeled a whistle with a second order differential equation as a Helmholtz resonator. The aeroacoustic sources were determined in two different ways: with the so-called jet-drive model and the discrete vortex model. They found very good agreement with their experiments with the first model when the labium was placed far from the orifice and with the second model when that distance was short. In both cases, they neglected the growth of the perturbations in the jet. Furthermore, they fitted some parameters or used from previous experiments, for example, they assumed a constant phase speed of the vortices in the case of the discrete vortex model. Paál and Vaik[20] carried out numerical simulations on the edge-tone and were able to reproduce various stages of the edge-tone, observed previously in their experiments.

Kobayashi *et al.*[16] carried out LES simulations and analyzed the effects of the acoustic and the hydrodynamic field on each other by Howe's energy corollary method.[13] They concluded that the sound is generated mainly in the second half of the oscillating jet in flue instruments. This means that if the perturbation field of the jet is modeled properly, the emitted sound can be predicted well, even if the wedge is ignored. Of course, such calculations are only useful, if the hydrodynamic feedback can be neglected. The next step to develop such a model was made by Takahashi *et al.*[26] They approximated the hydrodynamic velocity field with their own wavy jet model in which they slightly modify the Bickley profile by prescribing an analytical wavy shape of the fluctuating jet at the centerline. They modeled the growth of the hydrodynamic perturbation field with Fletcher's exponential models[9] with the common empirical assumptions so that the non-dimensional phase speed is 0.5 and the growth rate is equal to the wave number. The acoustic field was approximated by a single plane wave whose particle velocity has only a transversal component. They compared Howe's energy corollary integral at different domains in the mouth of the aperture and found a good agreement between their model and the result of a CFD simulation if they approximated the exponential growth by a Taylor series up to a cubic polynomial. Vaik *et al.*[29] made a thorough literature survey on how the frequency and the convection velocity can be estimated in the edge-tone and they also give a formula based on their previous experiments and simulation.[28] They found the phase velocity to vary between 1.58 and 0.19 over the streamwise distance which casts doubt on the usability of a constant value.

Jet modeling can be attacked by the previously mentioned linear stability analysis. It can provide disturbance fields with varying growth rates and also space-dependent phase velocities. Of course, this approach has the deficiency that it cannot model the hydrodynamic feedback in an edge-tone or in a flue instrument without further extensions.

New stability investigation methods were developed in the last few years. The parabolic stability equation[12] seems to be a promising method to model perturbations in the edge tone. It was applied to an axisymmetric jet by Garnaud *et al.*[11] However, the computation time is significantly higher here than that with the above-mentioned methods. If the number of assumptions is further reduced, the global stability methods are obtained. A comprehensive review about these techniques

was written by Chomaz.[5] They are powerful and sophisticated techniques but at the same time they need ample computational resources, which render their applicability in some flue instruments difficult, where the jet should be modeled in a wide range of frequencies.

We believe that if the modes of both the acoustic and hydrodynamic fields are calculated properly, then the interaction between them can be described. In this paper, we focus only on the hydrodynamic modes and in further research, we would like to take into account their interaction with acoustic waves using adjoint operators. The hydrodynamic modes are obtained by four different approaches. They, together with their solution method, are presented in Sec. II. In Sec. III, the model for acoustically excited incompressible flows will be presented and validated in a case when an acoustic wave passes over a no-slip wall. After that the CFD simulations of the base flow and the excited jet are described. In Sec. V, the results on the comparison of the different models with each other and with the CFD simulations are presented. Finally, concluding remarks are made in Sec. VI.

II. STABILITY EQUATIONS AND THEIR SOLUTION METHODS

In this paper, application of four different linear stability investigation methods on the plane jet are compared with each other. All of them are based on linearization of the continuity and the Navier-Stokes equations around a basic flow. The problem can be simplified, if a wavelike perturbation is assumed which has the following form in most of the investigated cases (except for the WKJB approximation):

$$\widetilde{u}_{ic,y}(x, y, t) = C_0 \phi(y) e^{i(\alpha x - \omega t)}, \tag{1}$$

or if the variation of the wave number is taken into account

$$\widetilde{u}_{ic,y}(x, y, t) = C_0 \phi(y) e^{i(\int \alpha(x)dx - \omega t)}, \tag{2}$$

where $\widetilde{u}_{ic,y}$ is the non-dimensional incompressible perturbation velocity field, C_0 is a constant, $\phi(y)$ is the eigenfunction, α is the non-dimensional wave number, ω is the non-dimensional angular frequency, x and y are non-dimensional co-ordinates, and t is the non-dimensional time. [The non-dimensionalization is defined later by Eq. (60).] This assumption leads to boundary value-eigenvalue problems of four different differential equations, namely: the Rayleigh equation, the Orr-Sommerfeld (OS) equation, its modification taking the transversal velocity component of the base flow into account, here called the Bajaj-Garg (BG) equation.[3] The last one is the extension of the OS equation, in which the problem is solved by the Wentzel–Kramers–Jeffreys-Brillouin (WKJB) approximation also known as the multi-scale method. It will be introduced briefly in Sec. II C.

A. Rayleigh equation

The Rayleigh equation (3) is the inviscid perturbation equation in fluid dynamics for a viscous or inviscid basic flow.

$$(\alpha U - \omega)(\phi'' - \alpha^2 \phi) - \alpha U'' \phi = 0, \tag{3}$$

where y is the transversal co-ordinate, α is the wave number, $\phi(y)$ is the amplitude of the perturbation velocity in the transversal direction, $U(y)$ is the streamwise component of the basic flow, and $\square'$ is the derivative with respect to y. All variables are non-dimensional. The problem is an eigenvalue problem. The proper eigenvalue pairs $\alpha \in \mathbb{C}$ and $\omega \in \mathbb{C}$ fulfill the boundary conditions. These boundary conditions were in our case $\phi(0) = 0$, representing sinuous modes and $\phi(y \to \infty) = 0$ meaning that the perturbation vanishes far from the centerline.

The problem is solved by a similar technique to the compound matrix method (CMM) which was originally applied by Ng and Reid[18] for the Orr-Sommerfeld equation and used here for the other equations, too. The idea is outlined only briefly. We transform our equation to be able to prescribe boundary conditions in the far field. Then the dispersion relation is obtained which ensures that the boundary condition is fulfilled at the centerline. The proper eigenvalue pairs of the problem (α, ω) have to be determined to satisfy that relation. During the solution, the integration of the differential equation is started from infinity (numerically far enough) and then the dispersion relation is evaluated at the centerline. The difference between the prescribed value and the actual value should be minimized by changing the eigenvalues by any root finding technique, e.g., the Newton-Raphson iteration method. If the proper eigenvalues are found, the dispersion relation is fulfilled and the iteration is finished. This technique to solve the boundary value problem is known as the shooting method.

The method is applied to the Rayleigh equation in the following way. Equation (3) can be rewritten in the form

$$\phi'' + a_1\phi' + a_2\phi = 0, \tag{4}$$

where $a_1 = 0$ and $a_2 = -\alpha^2 - (\alpha U'')/(\alpha U - \omega)$ and its general solution is

$$\phi = C_1\phi_1 + C_2\phi_2. \tag{5}$$

At infinity the equation takes the form, since $U(y \to \infty) \to 0$, $U''(y \to \infty) \to 0$,

$$\phi'' - \alpha^2\phi = 0, \tag{6}$$

and the solution can be obtained as

$$\phi_\infty = C_{1,\infty}e^{\lambda_1 y} + C_{2,\infty}e^{\lambda_2 y}, \tag{7}$$

where $\lambda_{1,2} = \pm\alpha$, and let $\phi_1 \sim e^{\lambda_1 y}$ and $\phi_2 \sim e^{\lambda_2 y}$. For a free shear flow, the perturbation velocity is assumed to be zero as y tends to infinity,

$$\lim_{y\to\infty} \phi = \lim_{y\to\infty} \phi' = 0. \tag{8}$$

This can be fulfilled only if $C_{1,\infty} = 0$ and also $C_1 = 0$, then the solution simplifies to

$$\phi = C_2\phi_2. \tag{9}$$

Let us transcribe the second-order differential equation into a first order differential equation system

$$\begin{bmatrix} \phi'' \\ \phi' \end{bmatrix} = \begin{bmatrix} -a_1 & -a_2 \\ 1 & 0 \end{bmatrix} \begin{bmatrix} \phi' \\ \phi \end{bmatrix} \tag{10}$$

or

$$\phi' = \mathbf{A}\phi, \tag{11}$$

where $\mathbf{A}$ is the coefficient matrix. If we want to prescribe boundary conditions as $y \to \infty$, then we have to normalize the variable ϕ with $e^{\lambda_2 y}$, which will be denoted with $\boldsymbol{\eta}$,

$$\boldsymbol{\eta} := \frac{\phi}{e^{\lambda_2 y}}. \tag{12}$$

The new equation system can be obtained as

$$\boldsymbol{\eta}' = \frac{\phi'}{e^{\lambda_2 y}} - \lambda_2\frac{\phi}{e^{\lambda_2 y}} = (\mathbf{A} - \lambda_2\mathbf{I})\boldsymbol{\eta}. \tag{13}$$

The initial conditions can be calculated from Eq. (9) as

$$\boldsymbol{\eta}_\infty = \begin{bmatrix} 1 \\ \lambda_2 \end{bmatrix}. \tag{14}$$

The boundary conditions in the far-field ($y \to \infty$) are fulfilled automatically, if the integration is initialized with these values. The boundary conditions in the near-field ($y = 0$) have to be enforced, that is, the (α, ω) eigenvalue pairs have to be determined. The symmetric boundary condition $\phi'(0) = 0$ can be expressed with the new variables as

$$D(\alpha, \omega) = \eta_1(0) = 0, \tag{15}$$

where η_1 is the first component of $\boldsymbol{\eta}$. This equation is the dispersion relation of the problem.

B. Orr-Sommerfeld and Bajaj-Garg equations

The Orr-Sommerfeld equation can be obtained if we neglect the streamwise variation and the transversal and spanwise components of the basic flow. It reads in the 2D and non-dimensional form

$$\phi^{(iv)} - 2\alpha^2\phi'' + \alpha^4\phi = \mathrm{iRe}\left\{(\alpha U - \omega)(\phi'' - \alpha^2\phi) - \alpha U''\phi\right\}, \tag{16}$$

where Re is the Reynolds-number which will be defined in Sec. IV. A similar equation can be derived, if the transversal velocity component (V) of the basic flow is not neglected, which was derived by Bajaj and Garg.[3] Both equations can be written in the form

$$\phi^{(iv)} = a_1\phi''' + a_2\phi'' + a_3\phi' + a_4\phi, \tag{17}$$

whose coefficients can be found in Table I. If $V = 0$, both equations are the same.

The solution method is similar to the previous case. It will be introduced here briefly, for further description, we refer to the study of Nagy and Paál[17] and the original studies of Ng and Reid[18] and Sengupta.[25] The fourth order equation is rewritten as a first order differential equation system, transformed into the compound variables $\boldsymbol{\eta}$ and then normalized ($\widetilde{\boldsymbol{\eta}}$) to be able to prescribe boundary conditions at infinity. The final differential equation system will be

$$\widetilde{\boldsymbol{\eta}}' = \begin{bmatrix} b & 1 & 0 & 0 & 0 & 0 \\ 0 & b & 1 & 1 & 0 & 0 \\ a_3 & a_2 & a_1+b & 0 & 1 & 0 \\ 0 & 0 & 0 & b & 1 & 0 \\ -a_4 & 0 & 0 & a_2 & a_1+b & 1 \\ 0 & -a_4 & 0 & -a_3 & 0 & a_1+b \end{bmatrix} \widetilde{\boldsymbol{\eta}}, \tag{18}$$

TABLE I. The coefficients for the OS equation and the BG equation in (17).

Coefficients	OS equation	BG equation
a_1	0	Re V
a_2	$2\alpha^2 + i\mathrm{Re}(\alpha U - \omega)$	$2\alpha^2 + i\mathrm{Re}(\alpha U - \omega)$
a_3	0	$-(\mathrm{Re}\, V'' + \alpha^2\, \mathrm{Re}\, V)$
a_4	$-(\alpha^4 + \alpha\,\mathrm{Re}\,(-i\alpha\,\omega + i\alpha^2 U + i U''))$	$-(\alpha^4 + \alpha\,\mathrm{Re}\,(-i\alpha\,\omega + i\alpha^2 U + \alpha V' + i U''))$

where $Q = \sqrt{\alpha^2 + iRe(\alpha U_{\inf} - \omega)}$, $b = \alpha + Q$, and $U_{\inf} = U(y \to \infty)$. The initial conditions are at infinity

$$\widetilde{\eta}_\infty := \begin{bmatrix} 1 \\ -(\alpha + Q) \\ \alpha^2 + \alpha\,Q + Q^2 \\ \alpha\,Q \\ -\alpha\,Q(\alpha + Q) \\ \alpha^2\,Q^2 \end{bmatrix}. \qquad (19)$$

The symmetry boundary condition $\phi'(0) = \phi'''(0) = 0$ can be expressed with the new variables as

$$D_s(\alpha, \omega) = \widetilde{\eta}_5(0) = 0, \qquad (20)$$

which has to be satisfied via the determination of the proper eigenvalue pairs. This calculation will be described in Sec. II D. Finally, the original $\phi(y)$ eigenfunctions can be obtained from the following equation:[18]

$$\eta_1 \phi'' - \eta_2 \phi' + \eta_4 \phi = 0. \qquad (21)$$

C. WKJB approximation

The previous solution techniques seek the solution in the simple waveform (1). This form can be extended with further terms in the WKJB approximation. The method was adapted to the linearized Navier-Stokes equations by Garg.[10] He added only one further term, which leads to the solution form

$$\widetilde{\psi}_{WKJB}(x, y, t) = (C_0 \Phi(y, x_1)) e^{i \int (\alpha_0 + \varepsilon\alpha_1) dx - i\omega t}, \qquad (22)$$

where $\widetilde{\psi}_{WKJB}$ is the stream function of the disturbance field and Φ is its eigenfunction. Here, only the necessary formulae are presented, the derivation can be found in the original work. ε is a small dimensionless parameter characterising the non-parallel nature of the basic flow. It expresses the ratio of slow scales x_1 (the streamwise variation of basic flow) and the fast scales x (propagation of the disturbance wave). $\varepsilon = 0$ corresponds to a fully parallel mean flow and the method leads to the Orr-Sommerfeld equation. The streamwise variation of free shear flows[10] (jets and boundary layers) $\varepsilon = 1/\sqrt{\mathrm{Re}}$.

Φ and α_0 may be obtained from the solution of the Orr-Sommerfeld equation at each axial location as if the basic flow were parallel. They are the same as those in the previous case. Although the Orr-Sommerfeld equation was solved for the transversal velocity component before, it does not cause any problem since

$$\widetilde{u}_{ic,y}(x, y, t) = -\frac{\partial \widetilde{\psi}(x, y, t)}{\partial x} = -\alpha\widetilde{\psi}(x, y, t). \qquad (23)$$

This means that the two variables and equations can be transformed into each other by a linear transformation. Hence, the eigenvalues are the same for both cases, while the eigenmodes differ only by a constant multiplier which can be taken into account through C_0.

Here, α_1 should be calculated to improve the accuracy of the Orr-Sommerfeld method that can be determined from the following relations:

$$\alpha_1 = \frac{\widetilde{a}_2(x_1)}{i\widetilde{a}_1(x_1)}, \qquad (24)$$

where

$$\widetilde{a}_1(x_1) = -\int_D (b_1\phi + b_2\phi'')\phi^\dagger dy, \qquad (25)$$

$$\widetilde{a}_2(x_1) = \int_D \left((b_1 + U'')\phi^\dagger + 2U'\phi^{\dagger'} + b_2\phi^{\dagger''}\right)\frac{\partial\phi}{\partial x_1}$$
$$+ \int_D \left((b_4\phi - 2i\phi''/\mathrm{Re})\frac{d\alpha_0}{dx_1} + b_3\phi' + V\phi'''\right)\phi^\dagger dy, \qquad (26)$$

$$b_1 = 2\alpha_0\omega - 3U\alpha_0^2 - U'' + 4i\alpha_0^3/\mathrm{Re}, \qquad (27)$$
$$b_2 = U - 4i\alpha_0/\mathrm{Re}, \qquad (28)$$
$$b_3 = -V'' - \alpha_0^2 V, \qquad (29)$$
$$b_4 = \omega - 3\alpha_0 U + 6i\alpha_0^2/\mathrm{Re}, \qquad (30)$$

and $\phi^\dagger$ is the eigenfunction of the solution of the adjoint problem. It can be calculated similarly to the eigenfunction of the original OS problem with the CMM method shown in Sec. II B. Only the coefficients will differ in (17) according to

$$a_1^\dagger = 0, \qquad (31)$$
$$a_2^\dagger = 2\alpha^2 + i\,\mathrm{Re}(\alpha U - \omega), \qquad (32)$$
$$a_3^\dagger = 2i\,\mathrm{Re}\,\alpha U', \qquad (33)$$
$$a_4^\dagger = -(\alpha^4 + \alpha\,\mathrm{Re}\,(-i\alpha\,\omega + i\alpha^2 U)). \qquad (34)$$

Furthermore, the eigenvalues of the Orr-Sommerfeld equation and those of the adjoint problem are the same for a spatial problem, thus only the eigenfunction should be recalculated. In Sec. V, the various solutions will be compared, based on the amplitude of fluctuating transversal velocity along the centerline. For the WKJB method, it can be calculated from the streamfunction as

$$\widetilde{u}_{WKJB,y} = -\frac{\partial\widetilde{\psi}_{WKJB}}{\partial x_1} =$$
$$= C_0 \left(\varepsilon\frac{\partial\phi}{\partial x_1} + (\alpha_0 + \varepsilon\alpha_1)\phi\right) e^{i \int (\alpha_0 + \varepsilon\alpha_1) dx - i\omega t}. \qquad (35)$$

D. Numerical procedures

The differential equations [(13), (18), and (21)] were solved by the Runge-Kutta-Cash-Karp method with an adaptive step size technique where the tolerated absolute and relative errors were set to 10^{-10}. This low value was necessary to solve the dispersion relation with the proper accuracy (10^{-6}). That was done by the Matlab built-in *fsolve* function which can handle non-linear complex-valued functions. The determination of the first eigenvalue is a challenging task; the dispersion relation was evaluated on complex α plane with a fine resolution at $\omega = 0.1$ and then the intersections of $D_{Re} = 0$ and $D_{Im} = 0$ were determined, where D_{Re} and D_{Im} are the real and imaginary parts of the dispersion relation, respectively. The eigenvalues were ordered according to the decreasing imaginary part of α. In the next step, x or ω was changed slightly and it was assumed that the eigenvalue changed only a little so that the solution procedure to fulfill the dispersion relation was initialized with the previously calculated α value. In the last case when the linear stability equations were solved with WKJB approximation, the integrals were evaluated using the trapezoidal rule of numerical integration.

III. MODELING ACOUSTICALLY EXCITED FLOWS

In many experiments, the jet is acoustically excited. The investigation of such configurations is numerically very difficult without the separation of the acoustic and hydrodynamic fields because the length scale of the acoustic wave is much larger than that of the hydrodynamic waves. This makes it difficult or impossible to create an optimum grid for numerical computations. The other problem is the different characteristic magnitude of the amplitudes of the perturbation. The typical amplitude of the pressure perturbation in acoustics is in the 20 μPa (0 dB)–200 mPa (100 dB) range, while in the hydrodynamic field, the typical pressure variation is around 1–100 Pa. Differences of a similar order of magnitude appear between the acoustic particle velocity and typical hydrodynamic velocity fluctuations.

In this section, a technique is presented to treat the excitation of an incompressible flow with a known acoustic field. One way coupling is assumed, meaning that the rotational hydrodynamic field (with a vector potential, solenoid) has no effect on the acoustic field (with a scalar potential, irrotational). Furthermore, the acoustic field is supposed to be described by the linear acoustic wave equation. The governing equations of compressible and incompressible flows are compared with each other with the aim to obtain the **full velocity field** (acoustic and hydrodynamic) in an incompressible simulation with the help of extra terms. The acoustic field is assumed to be known and to fulfill the governing equations by itself. The idea is similar to the Lighthill analogy, where the hydrodynamic pressure field is reproduced in an acoustic simulation but here we do exactly the opposite. Here, the acoustic pressure and its effects are reproduced in a hydrodynamic simulation. This way, the flow disturbed by an acoustic wave can be simulated in a unified framework.

The method is validated by compressible and incompressible CFD computations in which an acoustic wave passes over a no-slip wall. Our goal is to integrate the acoustic excitation into an incompressible flow simulation.

A. Modification of the continuity equation

The continuity equation in the general form is

$$\frac{\partial \rho}{\partial \hat{t}} + \nabla \cdot (\rho \hat{\boldsymbol{u}}) = 0, \tag{36}$$

where ρ is the density, $\hat{t}$ is the dimensional time, and $\hat{\boldsymbol{u}}$ is the dimensional velocity vector. Let us decompose the variables into acoustic (ac) and hydrodynamic (ic) part as

$$\rho = \rho_{ic} + \rho_{ac}, \tag{37}$$

$$\hat{\boldsymbol{u}} = \hat{\boldsymbol{u}}_{ic} + \hat{\boldsymbol{u}}_{ac}. \tag{38}$$

The mean value of the acoustic variables is zero, while the incompressible density has no fluctuating part ($\rho_{ic} = \rho_0$). After substitution (37) and (38) into (36), the following equation is obtained:

$$\frac{\partial \rho_{ac}}{\partial \hat{t}} + \rho_0 \nabla \cdot (\hat{\boldsymbol{u}}_{ic} + \hat{\boldsymbol{u}}_{ac}),$$
$$+ \rho_{ac} \nabla \cdot (\hat{\boldsymbol{u}}_{ic} + \hat{\boldsymbol{u}}_{ac}) + (\hat{\boldsymbol{u}}_{ic} + \hat{\boldsymbol{u}}_{ac}) \cdot \nabla \rho_{ac} = 0. \tag{39}$$

During an incompressible fluid flow simulation, the following equation

$$\rho_0 \nabla \cdot \hat{\boldsymbol{u}} = S_c \tag{40}$$

can be solved. Our task is to determine the S_c term, which substitutes the acoustic field. The term on the left-hand side (LHS) is equivalent to the second term in (39) and the further terms in (39) should be included in S_c,

$$S_c = -\frac{\partial \rho_{ac}}{\partial \hat{t}} - \rho_{ac} \nabla \cdot (\hat{\boldsymbol{u}}_{ic} + \hat{\boldsymbol{u}}_{ac}) - (\hat{\boldsymbol{u}}_{ic} + \hat{\boldsymbol{u}}_{ac}) \cdot \nabla \rho_{ac}. \tag{41}$$

Equation (41) can be further simplified. The incompressible velocity is divergence-free ($\nabla \cdot \hat{\boldsymbol{u}}_{ic} = 0$). The term $\rho_{ac} \nabla \cdot \hat{\boldsymbol{u}}_{ac}$ is a product of two small quantities which can be neglected if the acoustic field is assumed to be small. Two terms remain

$$S_c \cong -\frac{\partial \rho_{ac}}{\partial \hat{t}} - \hat{\boldsymbol{u}} \cdot \nabla \rho_{ac}. \tag{42}$$

Let us analyze the magnitude of the quantities. The first term scales as $\rho_{ac}/T = \rho c_0 / \lambda$, where T is the period time, c_0 is the speed of sound, and λ is the wavelength. The second term can be written as

$$(\hat{\boldsymbol{u}}_{ic} + \hat{\boldsymbol{u}}_{ac}) \cdot \nabla \rho_{ac} = \hat{\boldsymbol{u}}_{ic} \cdot \nabla \rho_{ac} + \hat{\boldsymbol{u}}_{ac} \cdot \nabla \rho_{ac}, \tag{43}$$

where the first terms scales as $\rho u_0 / \lambda$ and the second term is the product of two small quantities and can be neglected. u_0 is a typical speed of the flow. If

$$\frac{u_0}{c_0} = Ma \ll 1, \tag{44}$$

then the second term in Eq. (42) is negligible. Finally, the extra term for the continuity equation at low Mach-numbers becomes

$$S_c \cong -\frac{\partial \rho_{ac}}{\partial \hat{t}}. \tag{45}$$

Of course, Eq. (42) can also be implemented in most commercial software but the application of the approximation (45) is computationally more effective.

It is convenient to express (45) by the acoustic velocity. It was assumed that the acoustic field by itself fulfills the governing equations including the continuity equation

$$\frac{\partial \rho_{ac}}{\partial \hat{t}} + \rho_0 \nabla \cdot \hat{\boldsymbol{u}}_{ac} = 0 \tag{46}$$

and

$$S_c \cong -\frac{\partial \rho_{ac}}{\partial \hat{t}} = \rho_0 \nabla \cdot \hat{\boldsymbol{u}}_{ac}. \tag{47}$$

B. Modification of the momentum equation

The general momentum equation is in the case of a Newtonian fluid

$$\rho \frac{D\hat{\boldsymbol{u}}}{D\hat{t}} = \rho g - \nabla(p + \frac{2}{3}\mu \nabla \cdot \hat{\boldsymbol{u}}) + \nabla \cdot \left[\mu\left(\nabla \otimes \hat{\boldsymbol{u}} + (\nabla \otimes \hat{\boldsymbol{u}})^T\right)\right], \tag{48}$$

where $\frac{D}{Dt}$ is the total derivative with respect to time, p is the dimensional pressure, and μ is the dynamic viscosity.

The following equation is implemented generally in an incompressible fluid simulation solver if the viscosity is constant:

$$\rho_0 \frac{D\hat{\boldsymbol{u}}}{D\hat{t}} = \rho g - \nabla p + \mu \Delta \hat{\boldsymbol{u}} + S_m. \tag{49}$$

The difference between the two equations [the terms missing from (49)] should be included in the term (S_m), that is,

$$S_m = -\rho_{ac}\frac{D\hat{\boldsymbol{u}}}{D\hat{t}} + f(\mu), \tag{50}$$

where $f(\mu)$ contains the terms involving viscosity and assumed to be small since they are associated with bulk viscosity and to the temperature-related viscosity variation. The first term is also expected to be small since $\rho_{ac} \ll \rho_0$ and is also neglected in linear acoustics,

$$S_m \approx \mathbf{0}. \tag{51}$$

The full velocity field can be reconstructed by this approach in an incompressible simulation. Note that while the extra term (47) was prescribed within the domain, the boundary conditions for the compressible simulation represented the sum of the hydrodynamic and acoustic terms. The careful reader might wonder why we neglected the derived extra term in the momentum equation and did not neglect it in the continuity equation, although the two terms are of similar order of magnitude. The answer is the recognition that in the continuity equation this term is non-negligible compared with the zero on the right hand side, while in the momentum equation, it is negligible compared with the $\mathcal{O}(1)$ term standing on the right hand side. Numerical calculations confirmed the correctness of this derivation.

C. Application test: Acoustic wave a near a no-slip wall

The previously derived technique was tested on a case, where an acoustic wave passes along a wall. The problem was solved by compressible and incompressible numerical simulations and they are compared to an analytical solution[15] which is

$$\hat{\boldsymbol{u}}_{ac} = u_{ac,0}e^{i(\hat{\omega}\hat{t} - \hat{\alpha}\hat{x})}, \tag{52}$$

$$\hat{\boldsymbol{u}}_{ic} = -u_{ac,0}\, e^{-\hat{y}/\delta_{ac}} e^{i(\hat{\omega}\hat{t} - \hat{\alpha}\hat{x} - \hat{y}/\delta_{ac})}, \tag{53}$$

$$\delta_{ac} = \sqrt{\frac{2\nu}{\hat{\omega}}}, \tag{54}$$

where $\hat{u}_{ac,0}$ is the amplitude of the acoustic wave, δ_{ac} is the thickness of the acoustic boundary layer (known as viscous penetration depth or skin depth), $\hat{\omega}$ is the circular frequency, $\hat{\alpha}$ is the wave number, ν is the kinematic viscosity, $\hat{x}$ is the direction of wave propagation, and $\hat{y}$ is the normal co-ordinate to the wall [Fig. (1)], both co-ordinates are dimensional.

The numerical simulations were carried out in ANSYS CFX 16.2 assuming both compressibility and incompressibility. Two different boundary condition configurations were tested. In the first case, fluctuating velocity inlet boundary condition was applied at the left end of the channel and the pressure was prescribed at the other end. This configuration is more robust and the mesh dependence study and the comparison of incompressible and compressible simulations were carried out on this configuration. However, the prescribed fluctuating velocity enforces the proper amplitude in the full domain that makes it hard to investigate whether the derived equations are correct. Only the phase delay of fluctuation along the channel can be checked which is 0 in an incompressible simulation without the extra terms and non-zero in a compressible case. In the second case, prescribed fluctuating pressure boundary condition was applied at both ends. This configuration is similar to the excited jet considered in Sec. IV B and the effect of the previously derived extra terms can be investigated here. However, this configuration is numerically less robust. The further boundary conditions were the same and are shown in Fig. 1. At the bottom of the domain a no-slip wall, while at the top symmetry boundary condition was prescribed.

In the first case, the velocity inlet condition was a time-periodic function defined as

$$\hat{u}_{inlet,x}(\hat{y}, \hat{t}) = A_u \sin(\hat{\omega}\hat{t}), \tag{55}$$

where $\hat{u}_x$ denotes the velocity component in the x-direction and A_u is the amplitude of the excitation. The further velocity components are zeros. The prescribed relative static pressure[1] was set to 0 Pa. The main parameters of the simulation and mesh can be found in Table II.

The compressible and incompressible simulations were carried out with this configuration. The only difference between the two simulations was that in the incompressible
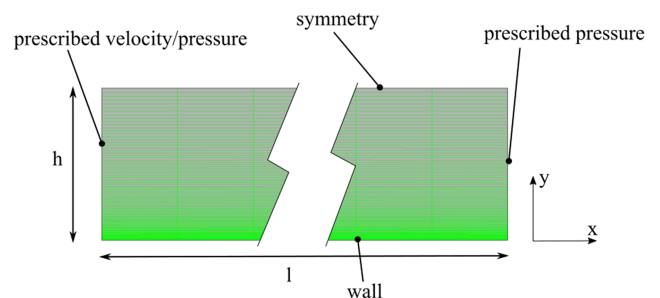

FIG. 1. The mesh for the investigation of the acoustic boundary layer and the boundary conditions.

TABLE II. The main parameters of the CFD simulations of the acoustic wave along a wall.

Name	Value
Length of the domain (l)	0.6 (m)
Height of the domain (h)	0.8 (mm)
Streamwise element size (dx)	0.4 (mm)
Transversal element size at the wall (dy_{min})	0.002 (mm)
Transversal element size far from the wall (dy_{max})	0.021 (mm)
Density	1.185 (kg/m^3)
Reference temperature	25 (°C)
Speed of sound (c)	346.2 (m/s)
Circular frequency of the sound wave ($\hat{\omega}$)	5 000 (rad/s)
Wave number of the sound wave ($\hat{\alpha}$)	14.42 (m^{-1})
Skin depth (δ)	0.078 74 (mm)
Turbulence model	Laminar flow was assumed
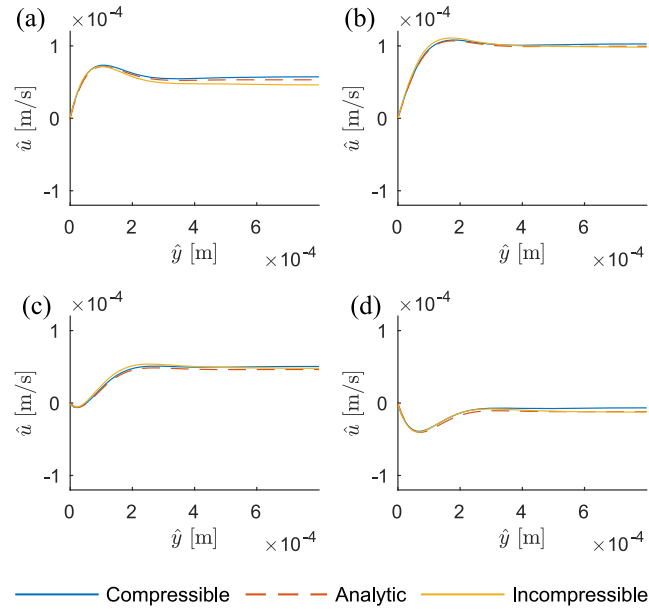
FIG. 2. The velocity profiles of the acoustic boundary layer along the $\hat{y}$ coordinate calculated in three different ways (with velocity inlet BC): with compressible, incompressible simulation (with extra term), and analytically in four different phases: (a) 0.61 rad; (b) 1.5 rad; (c) 2.7 rad; (d) 3.3 rad.

case, we included the previously derived extra term in the continuity equation. The velocity field was evaluated at a cross section in the transversal direction ($\hat{x} =$)0.3 m far from the inlet boundary. In Fig. 2, a very good agreement can be seen in all cases at every phase. The normalized root mean squared

deviation was calculated for the plotted phases as

$$\text{NRMSD}_u := \sqrt{\frac{\sum_{i=1}^{n}(\hat{u}_{anal,x}(\hat{y}_i) - \hat{u}_{CFD,x}(\hat{y}_i))^2}{n}} \frac{1}{A_u}, \quad (56)$$

where $\hat{u}_{anal}$ is the analytic solution and $\hat{u}_{CFD}$ is the numerical one. The NRMSD was around 0.02 in both simulations at all evaluated phases. Thus, the derived method above proved to be sufficient not only to generate the proper acoustic wave but also to reproduce the acoustic boundary layer in an incompressible simulation! With the help of this formula, the interaction between a hydrodynamic field and a known acoustic field can be investigated even in more complex cases in a single incompressible simulation, such as the acoustically excited jet, when an accurate compressible simulation cannot be carried out. (There are issues with non-reflective boundary conditions in the case compressible simulations, and the different scales also cause problems.)

1. Necessary grid resolution for the acoustic boundary layer

The necessary resolution of the acoustic boundary layer was also investigated. The number of elements in the y direction was varied between 34 and 100. The progression of their size was set to 1.025 in all cases. The results were compared with the analytical solution. A short phase delay was observed around 0.15 (rad). In order to handle this issue, a phase delay parameter was added to (52) and (53), and it was fitted to the numerical results. The largest difference between the analytical formula and the numerical results was normalized with the amplitude of excitation (u_0). The result can be found in Table III. The boundary layer should be resolved by about 20 elements if we want to keep the maximum error below 3%. At the same time, the root mean squared deviation decreased continuously with the size of mesh elements.

2. The effect of the length of the domain on the results

The effect of the length of the domain was carried out on the second configuration, where pressure was prescribed at both ends as

$$\hat{p}_{left}(\hat{y}, \hat{t}) = \rho_0 c A_u \sin(\hat{\omega}\hat{t}), \quad (57)$$

$$\hat{p}_{right}(\hat{y}, \hat{t}) = \rho_0 c A_u \sin(\hat{\omega}\hat{t} - \hat{\alpha}l). \quad (58)$$

The length of the domain was set to $l = \{0.01, 0.1, 0.435, 0.74, 1\}$ m with $dx = 1$ mm and the number of elements in the y direction was 75. Further parameters were the same as before. When the length of the domain is decreased and the extra term in the continuity equation was present, the accuracy

TABLE III. The comparison of the various meshes.

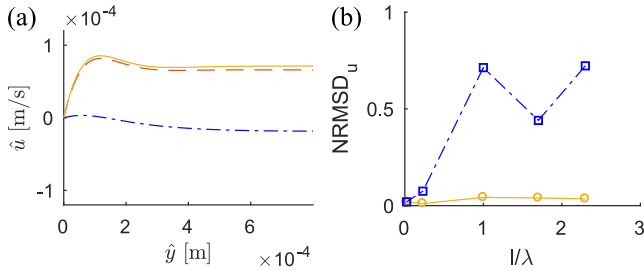| Case	1	2	3	4
Number of elements	100	75	54	34
Transversal element size at the wall (dy_{min}) (mm)	0.002	0.0038	0.0074	0.0159
Resolution of boundary layer (δ/dy_{min})	41.4	20.5	10.6	5.0
Normalized relative maximum difference (%)	2.32	2.63	3.45	5.82
NRMSD_u	0.0009	0.0012	0.0016	0.0027

(a)

(b)

FIG. 3. (a) The velocity profile of the acoustic boundary layer along the $\hat{y}$ co-ordinate in the phase 0.873 rad ($l = 1$ m). Analytical solution: dashed line, the incompressible simulation with the extra term (continuous line) and without the extra term (dashed-dotted line). (b) The normalized rms error compared to the analytic solution with (continuous line) and without (dashed-dotted line) the extra terms in the continuity equation.

of the simulation remained between 2% and 4% [Fig. 3(b)]. When this term was omitted, the error of the simulation was extremely high if $l/\lambda > 1$. However, it was just 7.5% for $l/\lambda = 0.23$ and 2% for $l/\lambda = 0.023$. This shows that, if the problem is acoustically compact ($l/\lambda \ll 1$), then the acoustic excitation can be modeled through boundary conditions even without the extra term. The reason for this is the phase delay in a compact configuration negligible, and thus the extra term has no significant effect on the simulation.

IV. THE CFD SIMULATIONS OF THE JET

A. The CFD simulation of the basic flow

The basic flow field of the plane jet was obtained with a steady 2D CFD simulation carried out with ANSYS CFX 16.2. The nozzle and the initial part of the jet were modeled in a half domain in order to avoid the spontaneous emergence of instability waves and to obtain faster convergence. In this way, the basic flow can be obtained even at larger Reynolds-numbers with the halved number of cells. The geometry, the mesh, and the boundary conditions are presented in Fig. 4. The nozzle length (l_n) was 7 mm, while its width (δ_n) was 1 mm (here only the half nozzle is shown because of symmetry). The length of the remaining domain (l) was 60 mm, and its height ($h/2$) was 25 mm. The mesh size was refined in 5 steps. The half nozzle was resolved with $n_{half} = 10, 20, 40, 60, 80$ elements [$\Delta y = \delta_n/(2n_{half})$] and above it the size of the elements was increased continuously with a quotient
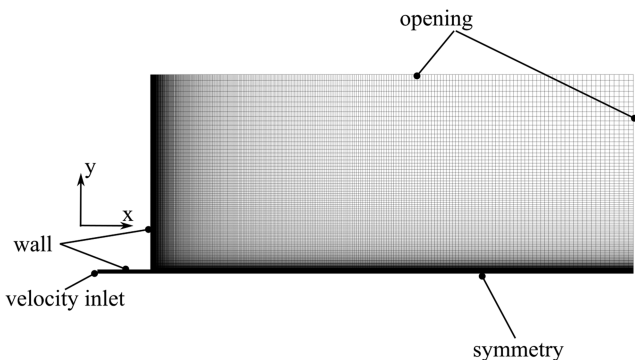
TABLE IV. The main parameters of the CFD simulations of the basic flow.

Name	Value
Length of the domain (l)	60 (mm)
Length of the nozzle (l_n)	7 (mm)
Height of the half domain ($h/2$)	25 (mm)
Width of the nozzle (δ_n)	1 (mm)
Density (ρ)	1.185 (kg/m^3)
Viscosity (ν)	1.545×10^{-5} m^2/s
Turbulence model	Laminar flow was assumed

1.03. At the nozzle, the other size of the cells was the same ($\Delta x = \Delta y$) and it was increased in both negative and positive directions with a quotient 1.01. At the nozzle left end, a parabolic velocity profile was prescribed. Its maximum was varied in order to obtain the basic flow at different Reynolds-numbers defined as

$$\text{Re} = \frac{\hat{U}_{mean}\delta_n}{\nu}, \qquad (59)$$

where $\hat{U}_{mean}$ is the mean velocity of the parabolic profile and $\nu = 1.545 \times 10^{-5}$ m^2/s is the kinematic viscosity. This definition also determines the length and time scales. The relation between dimensional (denoted with hat) and non-dimensional co-ordinates, wave number, angular frequency and time is

$$\hat{x} = \delta_n x, \ \hat{\alpha} = \frac{\alpha}{\delta_n}, \ \hat{\omega} = \frac{\omega \hat{U}_{mean}}{\delta_n}, \ \hat{t} = t\frac{\delta_n}{\hat{U}_{mean}}. \qquad (60)$$

The Reynolds-number was varied between 50 and 2000. Below these values, the edge-tone phenomenon is not observed, and above this range, the parabolic profile assumption in the nozzle is uncertain since it becomes unstable. At the nozzle wall and at the front wall, a no-slip wall boundary condition was prescribed, while at the centerline, symmetry boundary condition was applied. Opening boundaries were applied (see Fig. 4) at the remaining surfaces. Further settings are summarized in Table IV.

The mesh dependence study was carried out at each Reynolds-number. The imaginary part of α (α_i), which was calculated using the OS equation, was used for comparison at $\omega = 0.5$. The aim was that the maximum relative difference compared always to the finest grid at each location gets below

FIG. 4. The mesh and the boundary condition for the simulation of the basic flow.
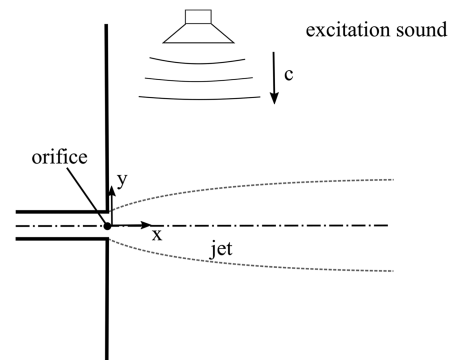

FIG. 5. The configuration of acoustically excited jet.

TABLE V. The parameters of the CFD simulations of the acoustically excited jet at various Reynolds-numbers.

Re	50	100	300	1000
$\hat{U}_{mean}$ (m/s)	0.7725	1.545	4.635	15.45
Mach-number	2.23×10^{-3}	4.46×10^{-3}	1.34×10^{-2}	4.46×10^{-2}
Time step (dt) (s)	2×10^{-4}	1×10^{-4}	3×10^{-5}	1×10^{-5}
Angular freq. of exc.(ω) (rad/s)	386.6	773.2	2320	7732
Wavelength of excitation (λ) (m)	5.626	2.813	0.9377	0.2813
Turbulence model	Laminar	Laminar	Various	k-ω
Skin depth of ac. wave (mm)	0.283	0.2	0.115	0.0632

1%. The outcome of this procedure was that the sufficient resolution of the orifice is $n_{half} = \{40, 40, 60, 60, 60\}$ at Re $\{50, 100, 300, 1000, 2000\}$.

B. The CFD simulation of the acoustically excited flow

As the next step, the acoustic excitation model was applied to the planar jet. Its configuration can be seen in Fig. 5. The jet flows in the x direction, while it is excited with transversally propagating acoustic waves. The geometry and the mesh were similar to the case of the basic flow simulation but here the full domain was modeled. Furthermore, the mesh parameter was set to $n = 20, 40, 60$ to investigate the effect of mesh resolution on the results. The Reynolds-number here was varied between 50 and 1000 but at 300 and above, the spontaneously developing unstable flow structures conceal the effect of excitation and the results cannot be evaluated with appropriate accuracy. Various turbulence models (k-ε, k-ω, shear stress transport[1]) were applied and tested to reduce this effect at Re = 300. This comparison will be shown later. The boundary conditions were also prescribed similarly to the unexcited case, only the pressure fluctuation was added to the "opening" boundaries. Further parameters can be found in Table V. The excitation was modeled as described in Sec. III with the differences that the acoustic wave propagated in the y direction and the pressure fluctuation was prescribed at the top and bottom of the domain. The Strouhal-number of the excitation was 0.5 in each case, while the particle velocity of the acoustic wave was set to $u_{ac,0} = 0.0001$ m/s.

The results were evaluated at monitor points placed along the centerline of the jet at every node and there the transversal velocity was recorded. A Fourier transformation was applied to the signals by Matlab 2017a, and the amplitude and the

phase delay were calculated at each location. The mesh dependence study was carried out based on these values at Re = 100. The amplitudes of these signals were compared with each other at the excitation frequency presented in Fig. 6(a). The curves cover each other, meaning that the results are in this range mesh-independent. The amplitudes were $\{7.333, 7.469, 7.513\}$ mm/s with the nozzle resolution: $n = 20, 40, 60$, respectively, at the location $x = \hat{x}/\delta_n = 10$. The relative difference was only 2.44% between the coarsest and finest grid and 0.59% between the medium and the finest grid. The same investigation was carried out at Re = 300. Unfortunately, in this case, the strong oscillation at other frequencies ruined the simulation and different solutions were obtained with different mesh resolutions. In this case, various turbulence models were tested and all of them solved the problem but the signal amplitudes were different in every case. The results can be seen in Fig. 6(b). The amplitude of the transversal velocity in the case of the laminar model on the coarse grid was the highest and it was in the same range for k-ω and shear stress transport turbulence models. At the same time, the k-ε turbulence model filtered out the oscillation and the calculated amplitude was more than one order of magnitude lower than in the other cases. It is difficult to determine which model provides the most accurate result; for further comparison, the k-ω turbulence model was selected.

V. RESULTS AND DISCUSSION

First, a hitherto unreported "strange" mode was found close to the flue channel using the OS equation. Its growth rate and phase speed are extremely high and it exists only there. Its phase speed tends to infinity and finally it disappears at $x \approx 1$. The existence of this mode can explain the high phase
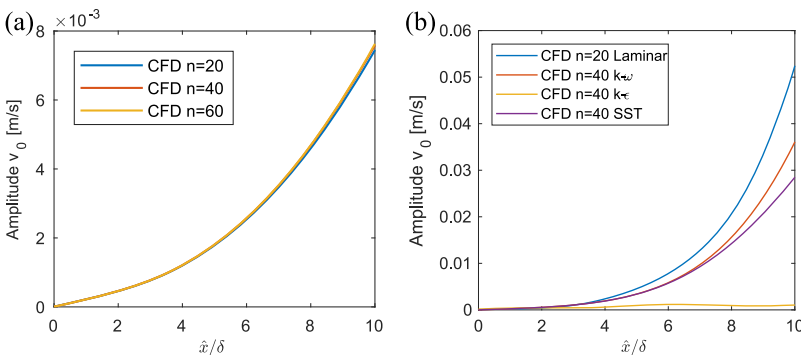

FIG. 6. The amplitude of the transversal velocity along the centerline of the jet at $\omega = 0.5$ (a) Re = 100 obtained with different mesh resolutions (n = {20, 40, 60}) (b) Re = 300 with various turbulence models.
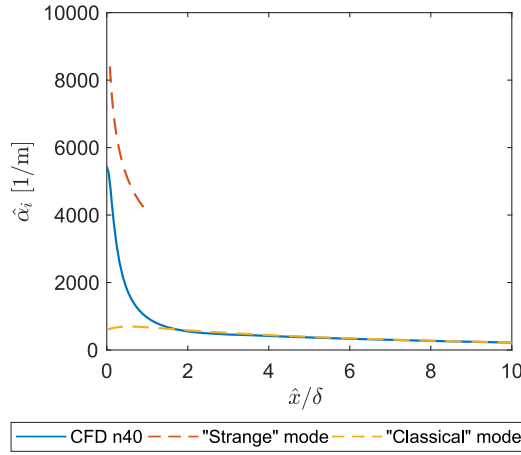
FIG. 7. The growth rate of the transversal velocity component along the centerline of the excited jet at St = 0.5, Re = 100.

FIG. 8. The amplitude of the transversal velocity component along the centerline of the excited jet at St = 0.5 (a) Re = 50, (b) Re = 100, (c) Re = 300, (d) Re = 1000.

speed found by Vaik et al.[28] during their numerical simulation. The growth rate of this mode and that of the "classical" mode, which exists also far downstream and is the most unstable one there, were compared to the CFD results in Fig. 7 at Re = 100. It can be seen that the growth rate calculated by the CFD simulations is between the two modes implying that the oscillation is the superposition of these two modes. Of course, the acoustic wave also excites the flow there, which makes higher growth rates than those calculated with the natural modes. (Since these modes are the eigenmodes and the excitation process was not taken into account.) The origin of this "strange" mode is unclear. If it is not caused by the numerical procedure and this mode emerges in real experiments, it can make hard to carry out measurements close to the orifice. Fortunately, this mode does not cause any problem in the modeling of the jet in the downstream region since these modes do not interact with each other if the linear assumption is valid and the strange mode exists only in the vicinity of the orifice.

Next, the reduced order models (Rayleigh, OS, BG, WKJB) were compared with the CFD results. The amplitudes and the phase delays of the fluctuating velocity along the centerline were compared to each other in all cases. These variables were selected for further comparison because they can be determined from the CFD simulation and they can be easily calculated from the eigenmodes by integration. If the growth rate or the phase speed variables had been selected for comparison, the numerical derivative would have had to be evaluated, leading to larger numerical errors. The unknown C_0 parameter in the eigenmodes was determined from the CFD results at $\hat{x}/\delta$ = 1.5 since upstream of that point the previously described "strange" mode makes the comparison difficult. Adjoint modes can help there but they will be the topic of further research.

The amplitude of the signal at the lowest Reynolds-number can be seen in Fig. 8(a). The results provided by the WKJB approximation are the closest to the CFD simulation, while the BG and OS models slightly underestimate the amplitude of the oscillation. If the Reynolds-number is increased from 50 to 100 [Figs. 8(a) and 8(b)], the difference between the results of the WKJB approximation and OS equation vanishes,
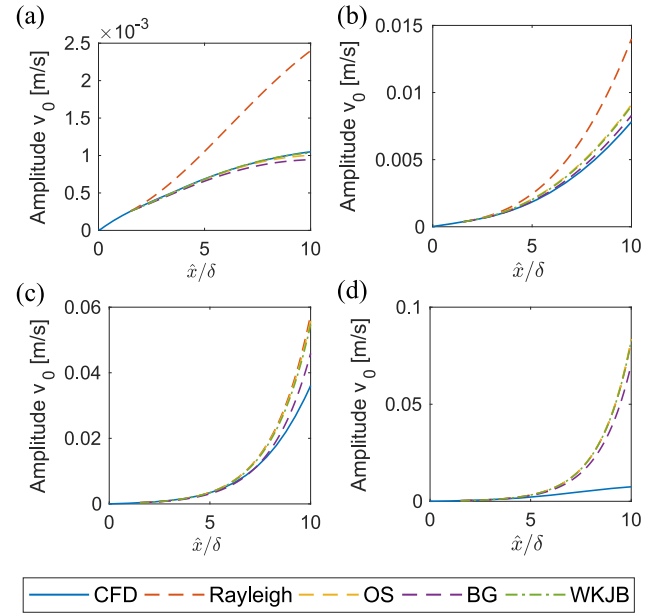
which holds for larger Reynolds-numbers, too. This was the expected result since the $\varepsilon = 1/\sqrt{\text{Re}}$. Thus the extra computational effort to obtain the α_1 correction terms is unnecessary for Re $\geq$ 100 and it has only a minor effect even below this value. At the same time, the BG model everywhere underestimates the growth rate compared to the others at Re = 50. In the case of Re = 100, the agreement is the best between this model and the CFD simulation. However, the difference between the models is small and according to our experience to solve the BG differential equation takes one order of magnitude more time than the OS equation. Furthermore, this model is inconsistent since it neglects the streamwise variation of the mean flow but takes into account the transversal velocity component of the basic flow. Therefore, this method is not recommended.

The Rayleigh equation predicts much stronger oscillation at Re = 50 and 100, indicating that the viscosity plays an important role at low Reynolds-numbers. If the Reynolds-number further increased (Re $\geq$ 300), the difference between the result provided by the Rayleigh and OS models becomes negligible. This conclusion was drawn by Curle[6] for the Bickley profile who suggests Re $\geq$ 200 for the inviscid domain. In this range, the k-ω turbulence model was applied in the CFD simulation which damped all the stray oscillations compared to the laminar case [Fig. 6(b)] and probably underestimates the magnitude of the oscillation.

Summarizing our conclusions about the amplitude, in the low Reynolds-number (50 $\leq$ Re < 300) range, the Orr-Sommerfeld equation is recommended since it is the second simplest method behind the Rayleigh equation and provides acceptable results. Above this regime (Re $\geq$ 300), the application of the Rayleigh equation is sufficient since it is computationally cheap and provides accurate results according to the experiments of Nolle.[19] No benefits are brought by the more advanced two methods.
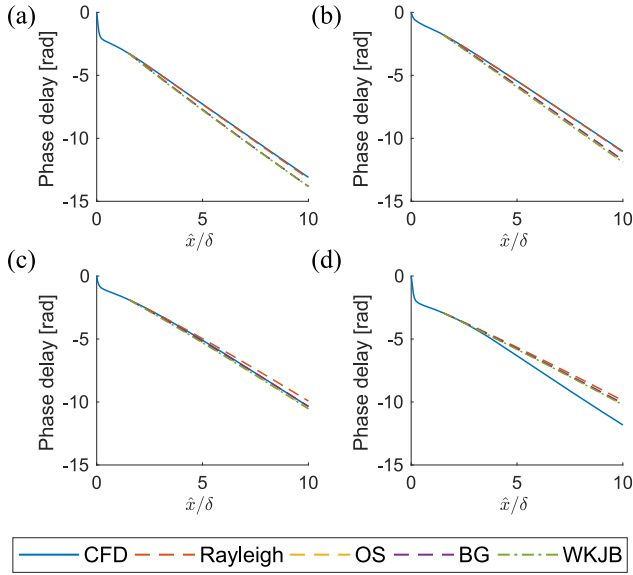
FIG. 9. The phase delay of the transversal velocity wave component along the centerline of the excited jet at St = 0.5 (a) Re = 50, (b) Re = 100, (c) Re = 300, (d) Re = 1000.

If the phase delay of the disturbance wave, whose spatial derivative is proportional to the phase velocity, is investigated, the results are surprising (Fig. 9). The phase delay is very well predicted by the Rayleigh equation when compared to the CFD simulations at $Re = \{50, 100\}$. Above those Reynolds-numbers, the results of the CFD simulations are questionable and the difference between the outcome of the different models vanishes. It is also remarkable that the phase delay is larger (the phase speed is smaller) in the models where viscosity was taken into account and the turbulence model further magnifies this difference [Fig. 9(d)].

A polynomial surface was fitted to the real and imaginary parts of the wave numbers at all Reynolds-numbers to approximate the growth rate and the phase speed better than the widely used values such as the non-dimensional phase speed being 0.5 and the growth rate being equal to the wave number. This procedure is shown in the Appendix.

Finally, the effect of the wall around the nozzle was investigated. Our original theory was at the beginning of the research that the different lengths and time scales of acoustic and hydrodynamic fields render a direct excitation impossible. Our idea was that the acoustic wave passes over the wall and generates vorticity whose length scale is comparable to the hydrodynamic field. This field can excite the jet. In order to test our theory, the wall around the nozzle (that is perpendicular to the jet) is switched from "no-slip wall" to "free slip wall." This setting prevents the development of the aforementioned hydrodynamic field and the excitation should become less effective. The comparison of the two cases can be seen in Fig. 10(a). The results clearly show that the change of boundary conditions has only a minor effect on the results. The amplitude was a bit larger in the case of a no-slip wall suggesting that the generated vorticity field also contributes to the excitation of the jet, but this effect is not as strong as originally assumed. The difference develops at the initial region since the growth rate of the transversal velocity was 10% larger close to the orifice
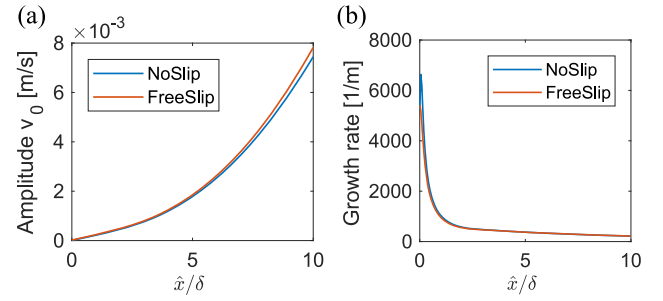

FIG. 10. The amplitude of the transversal velocity component (a) and its growth rate (b) along the centerline of the excited jet at St = 0.5, Re = 100 and the wall around the nozzle was switched from "no slip wall" to "free slip wall."

($x < 0.5$), but the growth rate values are almost the same in the downstream region ($x > 1$).

VI. CONCLUSIONS

A unified treatment of the flow and the acoustic excitation within an incompressible solver framework was presented and tested. It turned out that the vorticity, generated by the nozzle wall, plays only a minor role in the excitation process. Four different approaches, namely, the Rayleigh, the OS, BG equations, and the WKJB approximation, were implemented to predict the amplitude and the phase delay of the transversal velocity oscillation. The results show that the widely used Orr-Sommerfeld and Rayleigh equations are sufficient and the more sophisticated BG and WKJB methods provide no tangible benefit. The application of the OS equation is recommended below Re = 300 while that of the Rayleigh equation above this value. The latter one predicts both the growth rate and the phase velocity very well, independently of Re. A new instability mode existing only in the vicinity of the nozzle with extremely high growth rate was discovered.

APPENDIX: POLYNOMIAL FIT OF THE WAVE-NUMBER

The specific velocity and length scale of the jet change in the downstream direction and they also influence on the angular frequency. The model can be improved if this effect is compensated. Jo and Kim[14] found that the velocity distribution in the jet can be well described with $\xi = x/\text{Re}$. According to the self-similar solution of the Bickley-jet, the maximum velocity changes with $(\xi + \xi_0)^{-1/3}$ and the local length scale with $(\xi + \xi_0)^{2/3}$ meaning that the local time scale is proportional to $(\xi + \xi_0)$. ξ_0 is the location of virtual origin of the

TABLE VI. The coefficients of the fitted surface [Eq. (A1)] for real and imaginary parts of the wave number calculated with the Orr-Sommerfeld equation at different Reynolds-numbers.

Coefficients	$\Re(\alpha_L)$ Re = 50	$\Im(\alpha_L)$ Re = 50	$\Re(\alpha_L)$ Re = 100	$\Im(\alpha_L)$ Re = 100	$\Re(\alpha_L)$ Re = 300	$\Im(\alpha_L)$ Re = 300
p_{00}	0.014 798 1	−0.040 101	0.010 352 9	−0.017 536 4	0.011 753	−0.013 998
p_{10}	−0.088 058 4	−0.217 614	−0.054 342 2	−0.012 022 2	−0.512 052	0.133 51
p_{01}	8.223 42	−2.355 27	6.812 23	−5.968 33	4.913 47	−5.258 6
p_{20}	0.430 186	0.287 073	0.177 671	0.100 235	8.741 94	−1.494 52
p_{11}	0.376 817	8.144 88	−5.152 42	4.423 75	90.632 3	−46.642 1
p_{02}	−78.376 9	57.518 6	−31.565 4	180.715	−26.085 2	136.266
p_{21}	−17.214 5	−3.339 56	28.934 5	−5.740 55	−1 763.79	772.198
p_{12}	33.020 3	−137.659	20.236 2	−106.509	−2 704.81	4 156.18
p_{03}	472.376	−393.341	−105.133	−2 199.66	1 726.83	−2 894.19
p_{22}	201.192	20.330 2	−401.298	−341.553	68 477	−71 266.4
p_{13}	−441.781	852.38	719.065	1 504.2	−2 102.09	−46 204.1
p_{04}	−1 240.95	988.778	1 640.12	12 040.4	−28 351.9	38 834.4
p_{23}	−661.731	−55.238	1 050.24	4 650.61	−698 978	$1.073\,78 \times 10^6$
p_{14}	1 458.43	−1 669.32	−3 749.41	−10 592.7	403 424	−302 179
p_{05}	912.449	−625.732	−3 865.88	−2 213 4	80 721.6	−101 640
Max error	0.072 472 9	0.057 632 4	0.025 543 3	0.027 425 8	0.039 753 4	0.046 329 9
Rms error	0.005 393 27	0.016 833 9	0.006 623 98	0.008 157 95	0.005 366 38	0.006 584 25

jet and it is found to be 0.033 based on fit curves to the local length and velocity scales. The same value was suggested by Jo and Kim.[14] In order to account for the effects of the variation of local length and time scales, it is more convenient to give the approximation $\alpha_L = (\xi + \xi_0)^{2/3}\alpha$ as a function of $\omega_L = \omega(\xi + \xi_0)$ instead of α as a function of ω. The $\alpha_L(Re,\xi,\omega_L)$ function was approximated by a polynomial surface by Matlab *fit* function at different Reynolds-numbers. The data were taken from the following domain $\omega \in [0.005, 1], x \in [1, 15]$ and the spatial resolution was taken from CFD simulation and the resolution of ω was selected a way that the maximum relative difference between the two results is less than 2.5%. The order of the polynomial varied between 1 and 5. The most economic fit was achieved when the maximum order

of ξ was 2 and that of ω_L was 5 meaning the surface is described as

$$\begin{aligned}
\alpha_L(\xi,\omega_L) = \; & p_{00} + p_{10}\xi + p_{01}\omega_L + p_{20}\xi^2 \\
& + p_{11}\xi\omega_L + p_{02}\omega_L^2 + p_{21}\xi^2\omega_L + p_{12}\xi\omega_L^2 \\
& + p_{03}\omega_L^3 + p_{22}\xi^2\omega_L^2 + p_{13}\xi\omega_L^3 + p_{04}\omega_L^4 \\
& + p_{23}\xi^2\omega_L^3 + p_{14}\xi\omega_L^4 + p_{05}\omega_L^5.
\end{aligned} \tag{A1}$$

The coefficients are presented in Tables VI and VII also with the maxima and root-mean-square of the difference between the calculated and the fitted values. The maximum error was around 0.05, while the rms difference was below 0.01 almost in all cases.

TABLE VII. The coefficients of the fitted surface [Eq. (A1)] for real and imaginary parts of the wave number calculated with the Rayleigh equation at different Reynolds-numbers.

Coefficients	$\Re(\alpha_L)$ Re = 300	$\Im(\alpha_L)$ Re = 300	$\Re(\alpha_L)$ Re = 10^3	$\Im(\alpha_L)$ Re = 10^3	$\Re(\alpha_L)$ Re = 2000	$\Im(\alpha_L)$ Re = 2000
p_{00}	0.004 518 9	−0.006 381 69	0.000 212 36	−0.005 570 49	0.000 569 257	−0.004 110 56
p_{10}	−0.228 346	0.080 748 3	0.243 35	0.329 383	0.298 916	0.203 839
p_{01}	4.379 28	−5.531 51	6.325 78	−6.358 69	6.303 88	−6.980 15
p_{20}	4.761 93	−1.062 38	−13.419 8	−15.637 6	−30.473 1	−13.442 7
p_{11}	92.058 9	−45.399 8	−43.166 6	−117.885	−24.240 2	−76.009 5
p_{02}	−16.296 3	128.466	−254.01	314.609	−280.411	417.373
p_{21}	−1 740.07	779.375	3 650.51	5 598.04	5 602.83	4 001.58
p_{12}	−2 322.15	4 787.45	10 494.8	10 063.4	11 305.9	7 774.63
p_{03}	1 625.86	−2 948.91	12 313.2	−15 334.9	15 103.4	−22 408.8
p_{22}	59 875.5	−83 157.6	−619 508	−421 109	$-1.191\,87 \times 10^6$	−212 358
p_{13}	−8 339.17	−52 055.3	−134 514	−132 488	−46 066.4	−168 354
p_{04}	−26 584.4	42 493.5	−274 361	366 853	−385 052	590 352
p_{23}	−512 855	$1.273\,71 \times 10^6$	$1.205\,16 \times 10^7$	$4.197\,87 \times 10^6$	$1.842\,31 \times 10^7$	$-6.105\,3 \times 10^6$
p_{14}	333 124	−385 966	$-1.966\,01 \times 10^6$	998 968	$-3.396\,59 \times 10^6$	$4.667\,98 \times 10^6$
p_{05}	89 834	−105 818	$2.510\,77 \times 10^6$	$-3.257\,7 \times 10^6$	$3.891\,47 \times 10^6$	$-5.964\,49 \times 10^6$
Max error	0.045 945 8	0.062 647 1	0.034 607	0.022 839 3	0.020 349 5	0.007 738 63
Rms error	0.006 566 41	0.007 377 99	0.003 872 05	0.003 476 74	0.002 871 52	0.003 430 19

[1] ANSYS, Inc., *ANSYS 16.2 CFX Theory Guide*, 2015.

[2] Atassi, O. V. and Lueptow, R. M., "A model of flapping motion in a plane jet," Eur. J. Mech. B/Fluids **21**, 171–183 (2002).

[3] Bajaj, A. K. and Garg, V. K., "Linear stability of jet flows," J. Appl. Mech. **44**, 378 (1977).

[4] Bickley, W. G., "The plane jet," Philos. Mag. Ser. **23**(156), 727–731 (1937).

[5] Chomaz, J. M., "Global instabilities in spatially developing flows: Non-normality and nonlinearity," Annu. Rev. Fluid Mech. **37**(1), 357–392 (2005).

[6] Curle, N., "On hydrodynamic stability in unlimited fields of viscous flow," Proc. R. Soc. A **238**(1215), 489–501 (1957).

[7] Dequand, S., Willems, J. F. H., Leroux, M., Vullings, R., van Weert, M., Thieulot, C., and Hirschberg, A., "Simplified models of flue instruments: Influence of mouth geometry on the sound source," J. Acoust. Soc. Am. **113**(3), 1724–1735 (2003).

[8] Fabre, B. and Hirschberg, A., "Physical modeling of flue instruments: A review of lumped models," Acust. Acta Acust. **86**, 599 (2000).

[9] Fletcher, N. H. and Thwaites, S., "Wave propagation on an acoustically perturbed jet," Acust. Acta Acust. **42**, 323–334 (1979).

[10] Garg, V. K., "Spatial stability of the non-parallel Bickley jet," J. Fluid Mech. **102**, 127 (1981).

[11] Garnaud, X., Lesshafft, L., Schmid, P. J., and Huerre, P., "Modal and transient dynamics of jet flows," Phys. Fluids **25**(4), 044103 (2013).

[12] Herbert, T., "Parabolized stability equations," Annu. Rev. Fluid Mech. **29**, 245–283 (1997).

[13] Howe, M. S., "On the absorption of sound by turbulence and other hydrodynamic flows," IMA J. Appl. Math. **32**(1–3), 187 (1984).

[14] Jo, S. H. and Kim, M. U., "Hydrodynamic stability of two-dimensional jet near the nozzle exit," JSME Int. J. Ser. B **45**(3), 694–703 (2002).

[15] Kinsler, L. E., Frey, A. R., Coppens, A. B., and Sanders, J. V., *Fundamentals of Acoustics*, 4th ed. (John Wiley & Sons, New York, 2000).

[16] Kobayashi, T., Akamura, T., Nagao, Y., Nakano, K., and Takahashi, K., "Interaction between compressible fluid and sound in a flue instrument," Fluid Dyn. Res. **46**(6), 061411 (2014).

[17] Nagy, P. T. and Paál, G., "On the sensitivity of planar jets," Int. J. Heat Fluid Flow **62**, 114–123 (2016).

[18] Ng, B. S. and Reid, W. H., "An initial value method for eigenvalue problems using compound matrices," J. Comput. Phys. **30**, 125–136 (1979).

[19] Nolle, A. W., "Sinuous instability of a planar air jet: Propagation parameters and acoustic excitation," J. Acoust. Soc. Am. **103**, 3690–3705 (1998).

[20] Paál, G. and Vaik, I., "Unsteady phenomena in the edge tone," Int. J. Heat Fluid Flow **28**(4), 575–586 (2007).

[21] Rayleigh, J. W. S., *The Theory of Sound Perception* (Macmillan, 1896), Vol. 2.

[22] Sato, H., "The stability and transition of a two-dimensional jet," J. Fluid Mech. **7**(01), 53 (1960).

[23] Savic, P., "On acoustically effective vortex motion in gaseous jets," Philos. Mag. Ser. **32**(212), 245–252 (1941).

[24] Segoufin, C., Fabre, B., Verge, M. P., Hirschberg, A., and Wijnands, A. P. J., "Experimental study of the influence of the mouth geometry on sound production," Acust. Acta Acust. **86**, 649–661 (2000).

[25] Sengupta, T. K., *Instabilities of Flows and Transition to Turbulence* (CRC Press, 2012).

[26] Takahashi, K., Iwagami, S., Kobayashi, T., and Takami, T., "Theoretical estimation of the acoustic energy generation and absorption caused by jet oscillation," J. Phys. Soc. Jpn. **85**(4), 044402 (2016).

[27] Tatsumi, T. and Kakutani, T., "The stability of a two-dimensional laminar jet," J. Fluid Mech. **4**(03), 261 (1958).

[28] Vaik, I., Varga, R., and Paál, G., "Frequency and phase characteristics of the edge tone: Part I," Period. Polytech. Mech. Eng. **58**(1), 55–67 (2014).

[29] Vaik, I., Varga, R., and Paál, G., "Frequency and phase characteristics of the edge tone: Part II," Period. Polytech. Mech. Eng. **58**(1), 69–76 (2014).

[30] Varapaev, V. N., Shtemler, Y. M., and Yagodkin, V. I., "Effect of nonparallelism on the stability of a Bickley–Schlichting jet," Fluid Dyn. **8**(6), 966–968 (1975).